Published in "Review of Scientific Instruments 78(9): 093102, 2007"
which should be cited to refer to this work.

Relative detection efficiency of back- and front-illuminated charge-coupled device cameras for x-rays between 1 keV and 18 keV

J. Szlachetko,[a] J.-Cl. Dousse, J. Hoszowska, M. Berset, W. Cao, and M. Szlachetko
Department of Physics, University of Fribourg, CH-1700 Fribourg, Switzerland

M. Kavčič
J. Stefan Institute, SI-1001 Ljubljana, Slovenia

High-resolution x-ray measurements were performed with a von Hamos-type bent crystal spectrometer using for the detection of the diffracted photons either a back-illuminated charge-coupled device (CCD) camera or a front-illuminated one. For each CCD the main x-ray emission lines (e.g., $K\alpha$, $K\beta$, $L\alpha$, and $L\beta$) of a variety of elements were measured in order to probe the performances of the two detectors between 1 and 18 keV. From the observed x-ray lines the linearity of the energy response, the noise level, the energy resolution, and the quantum efficiency ratio of the two CCDs were determined.

I. INTRODUCTION

Since the 1970s, when the charge-coupled device (CCD) was invented at the Bell Telephone Laboratories,[1,2] the CCD has become a very efficient detector used in a variety of scientific areas (Ref. 3 and references therein). The CCD, which was originally developed as a memory device, presents indeed important advantages for x-ray detection: it provides high spatial and good energy resolution, has a relatively large detection area, and is characterized by an ultralow noise and a broad spectral response. In the last decades CCD detectors have been employed in an increasing way to supplant photographic films in astronomy and imaging as well as proportional counters and semiconductor detectors in x-ray spectroscopy (see, e.g., Refs. 4–7).

Nowadays a variety of commercial CCD systems are available, with different design architectures, sizes, and characteristics.[8–11] In general, CCD detectors can be divided up into two different types, namely, back- and front-illuminated devices.

In the case of front-illuminated cameras, the incoming x rays must first cross the dead layer corresponding to the polysilicon gate plus oxide layer before reaching the epitaxial layer of the CCD. Due to the absorption of the incoming radiation in the dead layer, the detection efficiency is somewhat diminished, depending on the energy of the x rays. As this absorption decreases with the energy of the incoming x rays, the efficiency of front-illuminated CCDs is first growing with increasing energies, but only as long as the incident photons can be fully absorbed in the depletion region. For higher energies the efficiency decreases. In addition, for x-ray energies tuned across the K edge of silicon there is an abrupt drop of the efficiency due to the sudden increase of the absorption coefficient of silicon at the K edge, which results in a stronger attenuation of the incoming photons in the dead layer. For instance, as reported in Ref. 12, the detection efficiency can drop down from about 80% for x-ray energies just below the edge to 25% for photon energies just above it, but in general the strength of this drop effect depends of course on the thickness and structure of the dead layer.

For back-illuminated CCDs the incoming x rays are entering the CCD directly from the side of the epitaxial layer. Therefore the detection efficiency is improved in comparison with the front-illuminated camera, especially in the energy range for which the absorption coefficient in Si is large. In general, the efficiency drop around the $1s$ absorption edge of silicon is also observed as a result of the unavoidable oxidization of the surface of the epitaxial layer but the drop is much less pronounced than that of front-illuminated CCDs. On the other hand, to avoid a too big absorption of photons in the field-free material region, the silicon wafer is chemically thinned, which limits the depletion depths of back-illuminated CCDs to $10-20$ μm. For this reason their efficiency is smaller compared to the front-illuminated CCDs for x-ray energies above about 4 keV.

In this article we report on results of extensive characterization measurements performed with a back-illuminated CCD and a front-illuminated one, both of scientific grade. The principal aim of the measurements was to probe and to compare the performances of the two detectors in the x-ray energy range between 1 and 18 keV. By measuring a variety of characteristic x-ray emission lines with a curved crystal spectrometer using the CCD devices for the detection of the diffracted x rays, we were able to determine the quantum efficiency ratio of the two cameras as a function of the x-ray energy as well as several characteristic parameters of the detectors such as the trailing and splitting effects, the linearity of the energy response, the energy resolution, and the noise level.

[a]On leave from Swietokrzyska Academy, Institute of Physics, 25-406 Kielce, Poland; electronic mail: jakub.szlachetko@unifr.ch

TABLE I. Characteristics of the employed crystals.

Crystal	$2d$ (Å)	Energy range (keV)
TlAP (001)	25.772	0.547–1.160
SiO_2 $(1\bar{1}0)$	8.5096	1.645–3.563
LiF (200)	4.0280	3.475–7.528
SiO_2 $(2\bar{2}3)$	2.7500	5.090–11.026
LiF (420)	1.8010	7.772–16.836

II. EXPERIMENTAL SETUP

A. von Hamos x-ray spectrometer

To characterize the two CCD cameras as a function of the x-ray energy, monochromatic x-ray radiation in the energy range from 1 to 18 keV was needed. The simplest solution would have consisted to irradiate the CCD detectors with monochromatic x-ray synchrotron radiation but the high intensity of synchrotron beams (typically $10^{10}-10^{12}$ photons/mm^2) was inadequate for the foreseen characterization measurements. In particular, single events per pixel were required, which was hardly feasible with synchrotron radiation. The characteristic x-ray emission lines of a variety of elemental and compound samples were therefore chosen as sources of monochromatic radiation. The fluorescence x-ray emission was produced by irradiating the samples with the bremsstrahlung of x-ray tubes. In order to probe the performances of the CCD detectors with well resolved $K\alpha$, $K\beta$, $L\alpha$, and $L\beta$ x-ray emission lines a wavelength dispersive instrument, namely, an x-ray crystal spectrometer, was employed. By design, the Fribourg von Hamos x-ray crystal spectrometer[13] is equipped with a CCD based x-ray detection system. As the two CCDs were planned to serve as x-ray detectors for this crystal spectrometer, the employed experimental setup represented some kind of a natural choice.

The Bragg angle domain covered by the von Hamos spectrometer extends from 24° to 61°. In order to measure x rays with energies ranging between 1 and 18 keV, five different crystals were employed. The crystal specifications and energy range covered by each crystal in first order of reflection are given in Table I.

Two different 100 kV/3 kW Coolidge-type x-ray tubes were used. The first one equipped with a scandium anode and a 150 μm beryllium window was employed for the measurements between 1 and 3.6 keV. For the measurements of higher energy x-ray lines, a gold anode x-ray tube with a 1000 μm beryllium window was used.

Most irradiated samples were high-purity (better than 99%) metallic foils or polycrystalline plates mounted on aluminum frames. The powder samples were prepared by dusting the material onto adhesive aluminium backings. For the Ar and Kr gaseous samples, a 10 mm diameter cylindrical gas cell was employed. The list of all employed samples is given in Table II.

B. CCD detection system

The main specifications of the employed front-illuminated (FI) and back-illuminated (BI) CCDs are quoted in Table III where the chip size, pixel resolution, depletion depth, noise, and full well capacity are given. Photographs of the two cameras are presented in Figs. 1 and 2. Both chips (front illuminated: LCX-TE/CCD-1024E1; back illuminated: MTE400B E2V MPP CCD 36-10) were manufactured by EEV (Ref. 11) for Roper Scientific[9] which provides complete CCD systems and related control electronics and software.

The CCDs were operated through a dedicated controller (ST-133 from Roper Scientific) at a rate of 1 MHz for the back-illuminated camera and 100 kHz for the front-illuminated one, which corresponded to readout times of 0.6 and 2.6 s, respectively, for full images and 16 bit signals per pixel. As both CCDs were used in the full frame mode, the cameras should be shielded from the incoming radiation during the readout operations. This was done with an x-ray shutter placed in front of the detector. The shutter which was developed for the von Hamos spectrometer consists of two superimposed metallic absorbers, a 0.5 mm thick stainless steel plate in the front and a 1.5 mm Al plate behind. During data collection, both plates move apart from the longitudinal axis of the CCD which coincides with the dispersive axis of the crystal spectrometer (see Fig. 1). The signals delivered by the controller to start and stop the data acquisition are also employed to open and close, respectively, the x-ray shutter. For this reason and because the time for opening and closing the shutter is 0.21 s, the central area of the CCD is exposed a little bit longer than the top and bottom parts.

For both cameras, the CCD chip sits on a cold finger which is mounted on a thermoelectric two-stage Peltier cooler. The Peltier elements are cooled with water at 5 °C. In order to diminish the dark current noise, for the present experiment the CCD chips were operated at −50 °C. In addition, to minimize the remanent pixel charges a dedicated cleaning procedure (*clean circles function*) was applied before each new frame acquisition. This function shifts the self-accumulated charges in the CCD array to the serial register and then discards them.

The data were collected in the so-called multiple-frame mode. Depending on the intensity of the measured characteristic x rays, the number of acquired images varied between 200 and 2000 with exposure times of 1–5 s per image. The latter were chosen as a function of the number of photons impinging on the CCD to avoid multiple hits in a single pixel. In order to get rid of the CCD dark charge pattern, a background image, which was recorded beforehand with the x-ray shutter closed, was subtracted from all acquired frames. After the subtraction of the background frame, all images corresponding to the same measurement were stored in a single file with the possibility of viewing or processing off line any individual frame.

Both CCDs were operated in the full speed-free run mode which is used for real-time sequential acquisitions of data. In this mode data collection is steered directly by the CCD hardware (controller) without any interaction with the computer. In the free run timing mode the shutter opens when the readout of the previous frame is completed, closes again after the preset exposure time, remains closed during the data readout and then opens again for the acquisition of the next image. This measuring cycle is repeated until the

TABLE II. Measured x-ray emission lines.

Energy[a](eV)	Element	Emission line	X-ray tube (kV/mA)	Crystal	Reflection order	Target
1040.98	Na	$K\alpha_1$	Sc 30/20	TlAP(001)	1	NaCl powder
1253.6	Mg	$K\alpha_1$	Sc 30/20	TlAP(001)	2	Metallic
1486.7	Al	$K\alpha_1$	Sc 30/20	TlAP(001)	2	Metallic
1557.45	Al	$K\beta_1$	Sc 30/20	TlAP(001)	2	Metallic
1739.98	Si	$K\alpha_1$	Sc 30/15	$SiO_2(1\bar{1}0)$	1	Polysilicon
1806.56	Sr	$L\alpha_1$	Sc 30/20	TlAP(001)	2	$SrTiO_3$ powder
1835.94	Si	$K\beta_1$	Sc 30/15	$SiO_2(1\bar{1}0)$	1	Polysilicon
1871.72	Sr	$L\beta_1$	Sc 30/20	TlAP(001)	2	$SrTiO_3$ powder
2013.7	P	$K\alpha_1$	Sc 30/20	$SiO_2(1\bar{1}0)$	1	Powder
2139.1	P	$K\beta_1$	Sc 30/20	$SiO_2(1\bar{1}0)$	1	Powder
2307.84	S	$K\alpha_1$	Sc 30/15	$SiO_2(1\bar{1}0)$	1	Powder
2464.04	S	$K\beta_1$	Sc 30/15	$SiO_2(1\bar{1}0)$	1	Powder
2622.39	Cl	$K\alpha_1$	Sc 30/15	$SiO_2(1\bar{1}0)$	1	KCl crystal
2815.6	Cl	$K\beta_1$	Sc 30/15	$SiO_2(1\bar{1}0)$	1	KCl crystal
2957.7	Ar	$K\alpha_1$	Sc 30/20	$SiO_2(1\bar{1}0)$	1	Gas
3190.5	Ar	$K\beta_1$	Sc 30/20	$SiO_2(1\bar{1}0)$	1	Gas
3313.8	K	$K\alpha_1$	Sc 30/10	$SiO_2(1\bar{1}0)$	1	KCl crystal
3589.6	K	$K\beta_1$	Sc 30/10	$SiO_2(1\bar{1}0)$	1	KCl crystal
3691.68	Ca	$K\alpha_1$	Au 20/10	LIF(200)	1	Metallic
4012.7	Ca	$K\beta_1$	Au 40/10	LIF(200)	1	Metallic
4090.6	Sc	$K\alpha_1$	Au 20/10	LIF(200)	1	Metallic
4460.5	Sc	$K\beta_1$	Au 30/10	LIF(200)	1	Metallic
4510.84	Ti	$K\alpha_1$	Au 20/10	LIF(200)	1	Metallic
4931.81	Ti	$K\beta_1$	Au 30/10	LIF(200)	1	Metallic
4952.2	V	$K\alpha_1$	Au 20/10	LIF(200)	1	Metallic
5414.72	Cr	$K\alpha_1$	Au 30/15	$SiO_2(2\bar{2}3)$	1	Metallic
5427.29	V	$K\beta_1$	Au 30/10	LIF(200)	1	Metallic
5898.75	Mn	$K\alpha_1$	Au 30/10	$SiO_2(2\bar{2}3)$	1	Metallic
5946.71	Cr	$K\beta_1$	Au 30/25	$SiO_2(2\bar{2}3)$	1	Metallic
6403.84	Fe	$K\alpha_1$	Au 30/10	$SiO_2(2\bar{2}3)$	1	Metallic
6490.45	Mn	$K\beta_1$	Au 30/10	$SiO_2(2\bar{2}3)$	1	Metallic
6930.32	Co	$K\alpha_1$	Au 30/10	$SiO_2(2\bar{2}3)$	1	Metallic
7057.98	Fe	$K\beta_1$	Au 30/10	$SiO_2(2\bar{2}3)$	1	Metallic
7478.15	Ni	$K\alpha_1$	Au 30/15	$SiO_2(2\bar{2}3)$	1	Metallic
7649.43	Co	$K\beta_1$	Au 30/10	$SiO_2(2\bar{2}3)$	1	Metallic
8047.78	Cu	$K\alpha_1$	Au 30/15	$SiO_2(2\bar{2}3)$	1	Metallic
8264.66	Ni	$K\beta_1$	Au 40/30	$SiO_2(2\bar{2}3)$	1	Metallic
8638.86	Zn	$K\alpha_1$	Au 30/20	$SiO_2(2\bar{2}3)$	1	Metallic
8652.5	Re	$L\alpha_1$	Au 50/20	LIF(420)	1	Metallic
8905.29	Cu	$K\beta_1$	Au 40/30	$SiO_2(2\bar{2}3)$	1	Metallic
9175.1	Ir	$L\alpha_1$	Au 30/20	$SiO_2(2\bar{2}3)$	1	Metallic
9572	Zn	$K\beta_1$	Au 30/20	$SiO_2(2\bar{2}3)$	1	Metallic
9713.3	Au	$L\alpha_1$	Au 50/30	LIF(420)	1	Metallic
10 010	Re	$L\beta_1$	Au 60/30	LIF(420)	1	Metallic
10 543.72	As	$K\alpha_1$	Au 50/30	LIF(420)	1	ZnAs powder
10 708.3	Ir	$L\beta_1$	Au 30/20	$SiO_2(2\bar{2}3)$	1	Metallic
11 222.4	Se	$K\alpha_1$	Au 40/15	LIF(420)	1	Powder
11 442.3	Au	$L\beta_1$	Au 60/30	LIF(420)	1	Metallic
11 726.2	As	$K\beta_1$	Au 60/30	LIF(420)	1	ZnAs powder
12 495.9	Se	$K\beta_1$	Au 50/30	LIF(420)	1	Powder
12 649	Kr	$K\alpha_1$	Au 60/30	LIF(420)	1	Gas
14 112	Kr	$K\beta_1$	Au 60/30	LIF(420)	1	Gas
15 775.1	Zr	$K\alpha_1$	Au 60/30	$SiO_2(2\bar{2}3)$	2	Metallic
17 479.34	Mo	$K\alpha_1$	Au 60/30	$SiO_2(2\bar{2}3)$	2	Metallic

[a]From Ref. 14.

TABLE III. CCD characteristics.

	Front illuminated	Back illuminated
Chip size	1024×256	1340×400
Pixel size	27×27 μm^2	20×20 μm^2
Epitaxial layer thickness	50 μm	~15 μm
Noise	3–7e^- at 100 kHz	8.5e^- at 1 MHz
Full well capacity	348 ke^-	201 ke^-

chosen number of frames is reached. Each new acquired image, after subtraction of the background frame, is displayed on the personal computer (PC) screen, which permits to have a live survey of the measurements.

C. CCD characterization parameters

In the following, a brief description of the main parameters used in the characterization of the employed CCDs is given.

Charge collection efficiency (CCE). The charge collection efficiency describes the capability of the channel capacitor to collect charges. The CCE depends, in particular, on the full well capacity, which gives the maximum number of electrons that can be trapped within a single pixel.

Charge transfer efficiency (CTE). The charge which is collected in a single pixel must be transported through the CCD array to the serial register and then to the preamplifier. During this transfer some fraction of the charge might get lost due to the mechanism of the charge transfer or the "design trap" effect reported in Ref. 3 The charge transfer efficiency is expressed as the ratio of the charge transferred from a pixel to the next one. For scientific grade CCDs, CTE values are very close to 1, typically 99.999%.

Quantum efficiency (QE). The quantum efficiency gives the ratio of the number of photons detected by the CCD to the total number of incoming photons. The QE of back- and front-illuminated cameras can be estimated by means of the following simple formulas:[3]

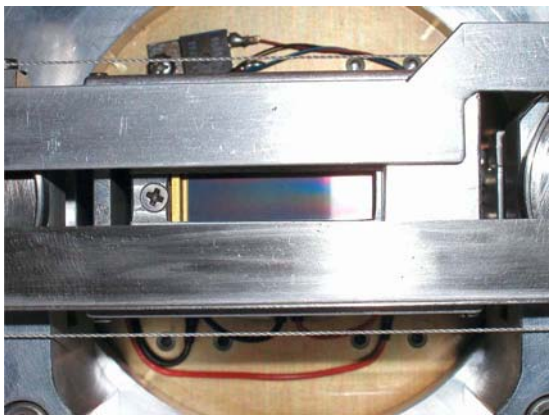

FIG. 1. (Color online) Photograph of the FI camera showing the CCD chip and x-ray shutter.

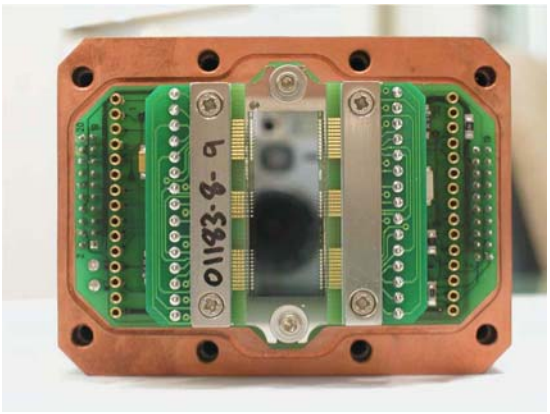

FIG. 2. (Color online) Photograph of the BI camera chip.

$$\mathrm{QE_{BI}}(E) = \mathrm{CCE}[1 - R(E)](1 - e^{-x_{\mathrm{Si}}/L_A(E)}) \tag{1}$$

or

$$\mathrm{QE_{FI}}(E) = \mathrm{CCE}[1 - R(E)](e^{-x_{\mathrm{SiO_2}}/L_A(E)})(1 - e^{-x_{\mathrm{Si}}/L_A(E)}), \tag{2}$$

where R is the reflection coefficient for silicon, CCE is the charge collection efficiency, and x_{Si} and $x_{\mathrm{SiO_2}}$ are the thicknesses of the depletion region and dead layer, respectively. The absorption length L_A is the inverse of the total photon attenuation coefficient for Si. R and L_A depend on the energy of the incoming photons.

Dark current. The dark current originates from thermal electron excitations. It strongly depends on the temperature of the CCD chip. For Si, the dark current decreases by a factor of 2 for every diminution of the temperature by 6 °C.[15] It can be noted that the surface dark current is significantly smaller in multipinned phase (MPP) CCDs,[16] a category of devices to which belongs the back-illuminated CCD used in the present study.

Readout noise. The total CCD noise, which is the noise measured at the output of the CCD camera system in the absence of any source of radiation, consists mainly of the above-mentioned dark current noise and the so-called readout noise (RN). The RN originates from the electronics of the CCD camera, being mainly due to the analog to digital converters (ADCs). Note that the contribution of the dark current to the CCD noise increases linearly with the CCD exposure time, whereas the readout noise does not depend on the exposure time.

III. DATA ANALYSIS AND RESULTS

A. 2D charge pattern

As a result of the interaction of the incoming x rays with the Si epitaxial layer electron-hole pairs are created. The number N of released electrons for the full absorption of an x ray of energy E is given by

$$N = \frac{E(\mathrm{eV})}{3.65}, \tag{3}$$

where the value of 3.65 eV corresponds to the energy required to form an electron-hole pair in silicon.

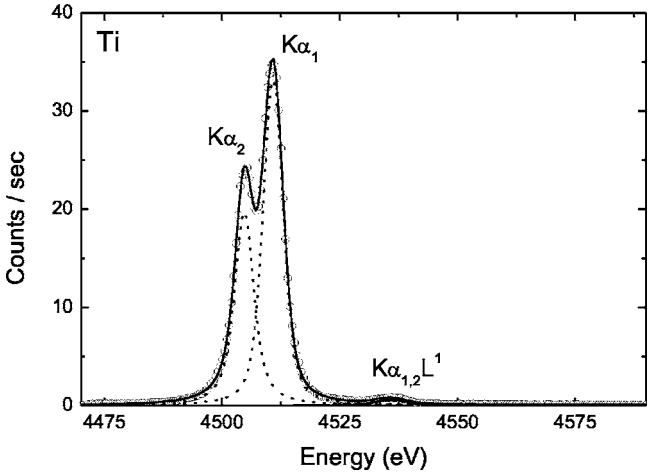

FIG. 3. High-resolution $K\alpha$ x-ray spectrum of Ti measured with the von Hamos spectrometer equipped with the FI camera.

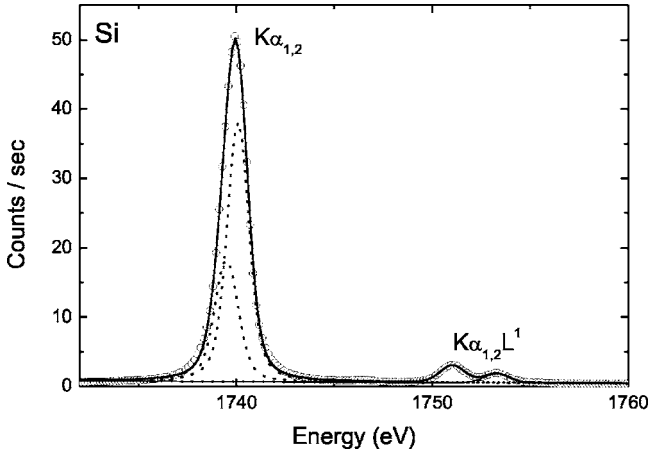

FIG. 4. High-resolution $K\alpha$ x-ray spectrum of Si measured with the von Hamos spectrometer equipped with the BI camera.

The released electrons are captured in the pixel potential wells and the corresponding trapped charges generate electronic signals which after amplification are converted into digital numbers. Representing these numbers by specific colors, a two-dimensional image can be constructed which reflects the charge pattern of the CCD as a result of its exposure to the x-ray radiation. In such images, the coordinates of the point correspond to the row and column numbers of the pixel and the color to the charge that was deposited in that pixel. Since the charge deposited in the pixels is proportional to the energy of the absorbed photons, good pixels can be sorted by filtering the data with an energy window. If the pixel charge fulfills the conditions of the energy window, a 1 is assigned to that pixel, if not a zero. This procedure reduces the number of background events originating from scattered photons, photons diffracted in higher orders by the crystal, or cosmic rays. The energy window can be determined from the frequency distribution of the charges deposited in the pixels. This histogram can be also used advantageously to probe the CCD performance or determine its characteristics. A more detailed description of the histograms and image filtering procedure is given in the next section.

In measurements performed with the von Hamos spectrometer the two-dimensional images corresponding to single exposures of the CCD are first filtered, using the appropriate energy window, and then summed together. Thanks to the spatial resolution of the CCD detector, the resulting total image presents vertical stripes corresponding to the different wavelengths, i.e., energies, of the x-ray radiation diffracted by the crystal according to the Bragg law. To obtain the corresponding high-resolution x-ray spectrum, the total image is finally projected onto the dispersive axis of the spectrometer which is parallel to the length direction of the CCD. For illustration, the high-resolution $K\alpha$ x-ray spectra of Ti and Si measured with the FI and BI cameras, respectively, are shown in Figs. 3 and 4. The resolved weak x-ray structures occurring in these spectra at about 4535 and 1752 eV correspond to the first order L satellites of the $K\alpha$ transitions, i.e., to the $2p$-$1s$ transitions with one additional spectator vacancy in the L shell.

B. CCD histograms

In Figs. 5 and 6 two examples of histograms are presented. Selected areas of the corresponding two dimensional (2D) CCD images are shown in the insets. The histograms correspond to the above-mentioned Ti $K\alpha$ and Si $K\alpha$ measurements. In both histograms, pixel charges are expressed in e^-. The conversion factor between the digital numbers given by the ADCs and the corresponding pixel charges in e^- was determined using Eq. (3) and the energy responses of the CCDs discussed at the end of this section.

The 2D image of the FI camera shows that each event consists of a main pixel accompanied by a horizontal tail of several pixels on the left. This trailing effect appears in the corresponding histogram as a series of peaks shifted to lower charge values. A similar observation reported in Ref. [3] was explained by a poor charge transfer efficiency due to a design trap problem. We have found that, independent of the measured x-ray energy, the positions of the secondary peaks are always shifted down by a factor of about 0.6 with respect to the next peak above. The length of the tails is always the

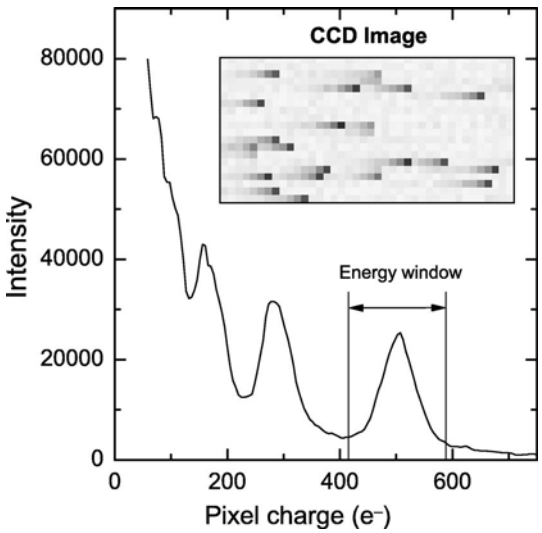

FIG. 5. Histogram of the charge distribution in the FI CCD. The histogram was constructed from the measurement of the Ti $K\alpha$ x-ray spectrum. In the inset, a selected area of a 2D image is shown.

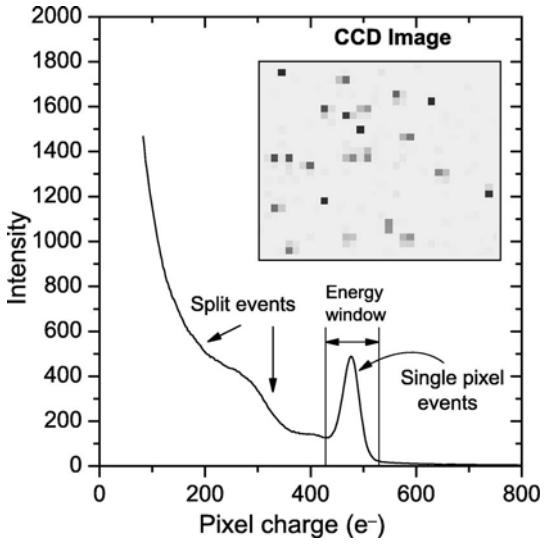

FIG. 6. Histogram of the charge distribution in the BI CCD. The histogram was constructed from the measurement of the Si $K\alpha$ x-ray spectrum. In the inset, a selected area of a 2D image is shown.

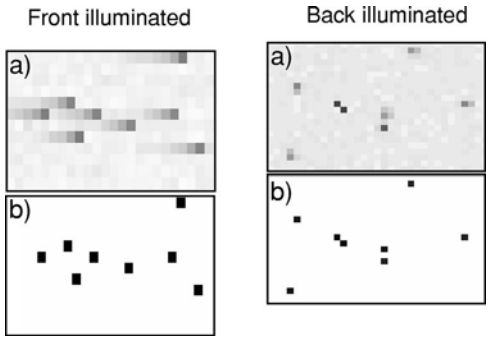

FIG. 7. Selected areas of raw (a) and corrected (b) images of the FI and BI cameras.

same, no matter on which part of the CCD the photon is absorbed, but for increasing photon energies the tail length grows. This implies that the design trap should be located between the last polysilicon gate (transfer gate) and the serial register. A plausible explanation for the charge trailing is that the ends of the channel stops on the side of the serial register were designed wider in order to better guide the charges to the register. Due to that, a small potential difference between the last gate and the transfer gate occurs which can hold back several hundreds of electrons.[3] Note that the observed tails are horizontal because for the FI camera the serial register is vertical. As indicated by the histogram, in our case the percentage of electrons trapped by this parasitic potential is about 60%. In other words, only 40% of the charge deposited originally in the hit pixel is forwarded to the controller. During the next transfer 40% of the "delayed" charge, i.e., 24% of the original one, will be assigned by the controller to the next pixel although the latter had no charge in the real CCD image. This erroneous attribution of charges to empty pixels during the readout process continues until the wrong signals become negligibly small and disappear in the noise. To determine the real charge deposited in the single hit pixel (the one with the biggest charge), one should thus sum the charges of all neighbor pixels belonging to the trailing event.

A completely different behavior is observed for the BI camera. As shown by the inset of Fig. 6, in this case the charges are either deposited in single pixels or split randomly between several neighbor pixels. This charge splitting effect[3] occurs when a photon is absorbed in the field-free region. Due to the weak electric field existing in this region, the electron cloud can indeed diffuse over an area corresponding to several pixels before being trapped by the potential wells of different pixels. Therefore, the corresponding histogram contains a small peak which corresponds to the single event pixels and a broad structure arising from the split events. Of course, the image filtering process can be performed using an energy window corresponding to the single event peak of the histogram,[7] but this leads to a significant loss in the detection efficiency. It can be noted here that split event pixels are rarely observed in images taken with the FI camera, except for the highest photon energies. This is due to the design of the FI CCD in which the field-free region is located opposite the exposed side of the chip, after the depletion region. As a consequence, only few x rays and only those with a high enough energy can reach the field-free region where the charge splitting takes place.

In order to recover the charges lost as a result of the trailing and splitting effects observed with the FI and BI cameras, dedicated image processing codes were developed. For the images taken with the BI camera, the code determines first the average charge of the single event pixels. Then the charges corresponding to the split event pixels are summed up with the condition that the obtained sum should be consistent within the experimental uncertainty with the average charge of the single event pixels. Finally the total charge is assigned to the pixel with the highest partial charge. As in most examined 2D images, the major part of the charge was found to be shared between four neighbor pixels or fewer, a maximum of four pixels is taken into consideration by the code in the sum of the split charges. For FI images, a similar code was developed. In this case, the charges of the tail pixels are summed and the total charge is assigned to the first pixel on the right of the tail. If split event pixels are present, their charge is accounted for in the sum. For illustration, selected areas of raw and processed 2D images are shown for both cameras in Fig. 7.

The drastic improvements brought by the two image processing codes are illustrated by the Figs. 8 and 9, where the histograms before (red line) and after (blue line) correction are shown. In Fig. 8, the histogram of the raw data corresponding to the measurement of the P $K\alpha$ x-ray line performed with the BI camera does not show any significant single event peak that could be assigned to the $K\alpha$ transition of phosphorus. Actually, the small peak observed at about $480e^-$ corresponds to the $K\alpha$ transition of silicon. According to Eq. (3), this Si transition is indeed expected at $477e^-$. As the energy of the P $K\alpha$ x-rays lies just above the K-shell ionization energy of silicon, the weak peak is due to the self-absorption in the epitaxial layer of the Si $K\alpha$ x-rays induced by photoionization in the CCD material by the incoming characteristic x rays of phosphorus. However, as shown by the blue line in Fig. 8, the single event peak corresponding to the P $K\alpha$ line is clearly resolved after correction of the

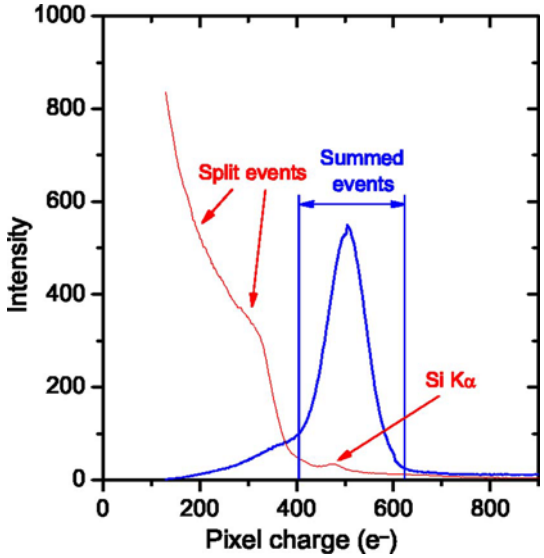

FIG. 8. (Color online) Histogram of the charge distribution in the BI CCD resulting from the measurement of the P $K\alpha$ x-ray spectrum. The red line corresponds to the histogram of raw data, the blue one to the histogram of corrected data (for details, see the text).

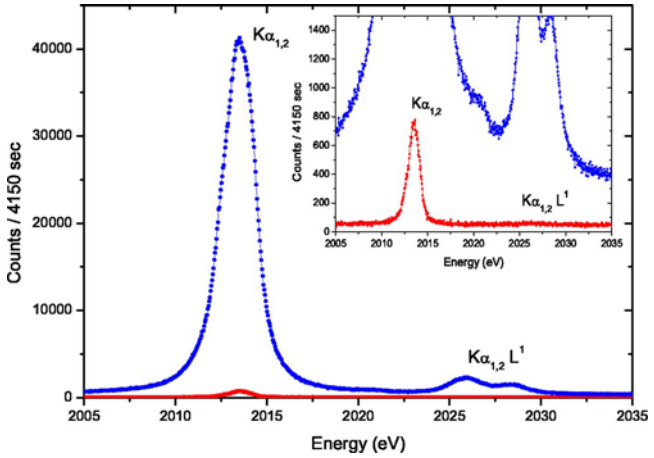

FIG. 10. (Color online) High-resolution $K\alpha$ x-ray spectrum of phosphorus measured with the von Hamos spectrometer equipped with the BI CCD camera. Red points stand for the raw spectrum, blue ones for the spectrum obtained after correction of the 2D images with the code discussed in the text. As shown in the inset, the x-ray satellite structure between 2022 and 2032 eV which is hardly visible in the uncorrected spectrum is well resolved from the background in the corrected one.

raw data with the above-mentioned image processing code. The fitted peak position (at 504e^-) corresponds satisfactorily to the theoretical value of 551e^- given by Eq. (3). The difference arises from events that were split into more than four pixels, i.e., from the residual charges that were not considered by the code in the computation of the total charge. Actually, the asymmetry occurring on the low-charge side of the peak is due to the charges of these omitted pixels.

As shown in Fig. 9 where the histogram corresponding to the measurement of the $K\alpha$ transition of aluminium is depicted, the correction software for images collected by means of the FI CCD is especially useful for low energy x rays. In the uncorrected histogram (red line), the Al $K\alpha$ peak corresponding to the pixels with the largest charge is partly

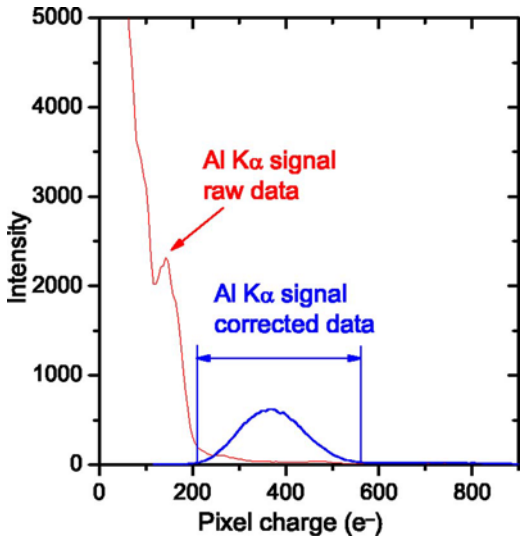

FIG. 9. (Color online) Histogram of the charge distribution in the FI CCD resulting from the measurement of the Al $K\alpha$ x-ray spectrum. The red line corresponds to the histogram of raw data, the blue one to the histogram of corrected data (for details, see the text).

overlapping with the tail of the electronic noise and with the peak associated to the first pixels on the left, i.e., the pixels with the second highest charge. Usually a width of 3σ is chosen for the energy window. However, if such a width is employed for filtering the unprocessed images, noise events will be sorted as good events with the result of a strong increase of the background in the high-resolution x-ray spectrum. On the other hand, the use of a narrower energy window leads to a significant loss of good events, i.e., to a diminution of the intensity of the transition of interest in the high-resolution x-ray spectrum. No such difficulty is encountered with the corrected histogram (blue line) in which a single peak is observed which is well resolved from the electronic noise. The centroid position found for the peak is 373e^-, in good agreement with the value of 407e^- obtained from Eq. (3).

The histograms of both CCDs are clearly improved by the two image processing codes. In particular, the peaks corresponding to the signals of interest are better resolved from the noise, which makes the choice of the appropriate energy windows easier. An example of the improvement brought by the correction software to the final x-ray spectra is shown in Fig. 10 for the BI camera. The price to pay for this improvement is some deterioration of the energy resolution of the CCDs. Comparing for instance the relative resolution of the peaks presented in Figs. 5 and 9 (FI camera) and in Figs. 6 and 8 (BI camera), respectively, one sees indeed that the relative charge or energy resolution becomes worse by a factor of about 3 for the FI camera and a factor of about 2 for the BI camera after the image processing. This worse resolution implies the use in the data analysis of wider energy windows, which in turn results in some enhancement of the background in the final high-resolution x-ray spectra. The main reason for the resolution loss resides in the fact that in the correction process the uncertainties on the charges of all summed pixels are added together.

The above discussed charge trailing and charge splitting

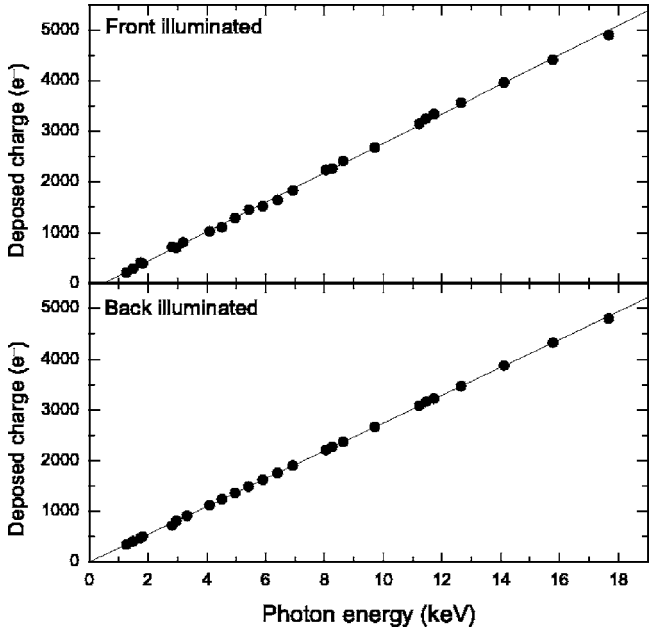

FIG. 11. Charge deposited in the two CCDs as a function of the photon energy. Experimental values are represented by full circles. Both sets of measured data were fitted with a linear function (solid line).

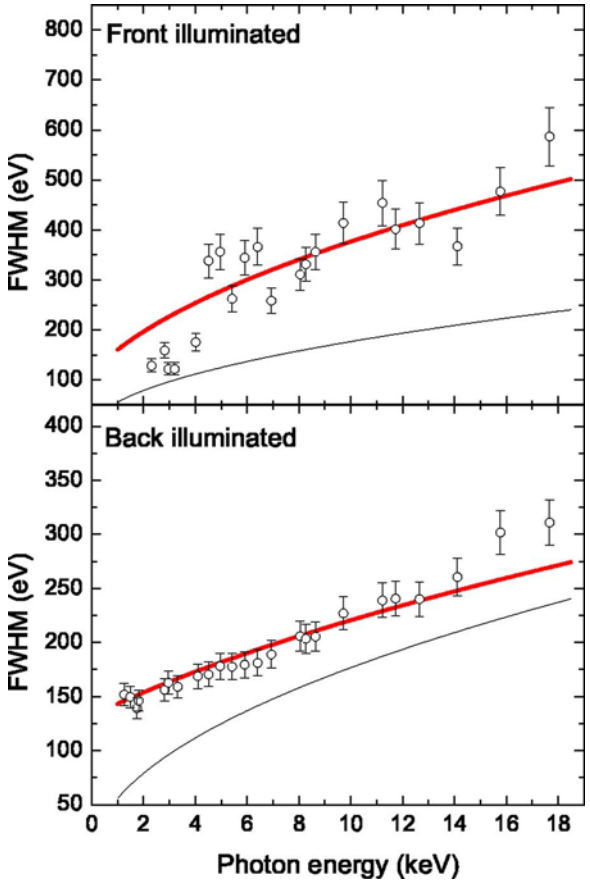

FIG. 12. (Color online) The energy resolution of the two CCDs as a function of the photon energy (open circles). The red solid lines correspond to the theoretical fits (see text), whereas the black solid lines represent the Fano limits (σ_N=0).

effects would make difficult the use of the two CCDs for the direct measurement of a polychromatic x-ray source. In particular, low x-ray energy spectra would be hardly measurable. Due to the presence of different energies in the incoming x rays, many peaks would be indeed overlapping in the histograms, which would make the use of correction codes as those presented above hopeless. In this case, the single possibility would consist choosing an energy window corresponding to the peak of the single event pixels for the BI camera and the peak of the pixels with the highest charge for the FI camera with the result, however, that the efficiency of the two CCDs would then decrease dramatically.

To determine the energy response of the two CCDs, the $K\alpha$ transitions of a variety of elements ranging from Mg (E=1.254 keV) to Mo (E=17.479 keV) were measured with the von Hamos spectrometer. The obtained 2D images were corrected to account for the trailing and split events, and for each measurement the corresponding histogram was constructed. The centroid positions of the resolved charge peaks occurring in the histograms were determined by means of a least-squares fitting procedure, using for each peak a single Gauss function. Results are plotted as a function of the transition energy in Fig. 11. As shown, the experimental points could be well fitted with straight lines, showing that the energy response of both CCDs is linear over the energy range of 1–18 keV. The slopes found for the straight lines are 274e^-/keV (BI) and 295e^-/keV (FI). Noticing that the inverse of the slope should correspond to the energy required to form an electron-hole pair in Si, values of 3.65 and 3.39 eV are found for the BI and FI cameras, respectively. The deviation of about 7% observed for the FI camera is probably due to the fact that split events and tail events with the smallest charges were not considered by the correction code for the FI CCD. For the same reason, the FI straight line does not converge exactly to the origin.

For each measured energy, the noise event histogram was derived and the corresponding standard deviation σ_N determined. Average σ_N values of 13.2e^- (FI) and 12.2e^- (BI) were found. Both results are bigger than the noise levels given in the CCDs specifications (see Table III). The increased noise is principally due to the presence in the vicinity of the CCDs of a turbo pump and several stepping motors.

From the same $K\alpha$ measurements, the energy resolution [full width at half maximum (FWHM)] of the two CCDs was determined as a function of the photon energy. The results are shown in Fig. 12. For the BI camera, the FWHM was estimated to be about 180 eV at a photon energy of 5.9 keV (Mn $K\alpha$ line). This result compares very well with the resolution of a good semiconductor detector (i.e. 150 eV at 5.9 keV; see, e.g., Ref. 17). The resolution of the FI camera is much poorer (344 eV at 5.9 keV) because of the CTE problems. As already mentioned only about 40% of the collected charge is transferred from the imaging area to the serial register. As a consequence, an additional uncertainty is introduced in the measurement of the electronic signal causing a broadening of the FWHM. To understand the photon energy dependence of the FWHM, the following formula was employed to fit our data:

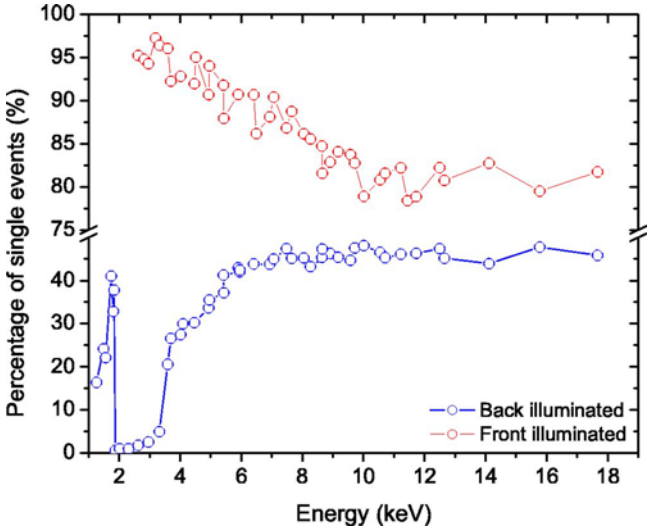

FIG. 13. (Color online) Percentages of events detected in a single pixel as a function of the incoming photon energy. Red open circles stand for FI data, blue ones for BI data.

$$\mathrm{FWHM} = 2.35 \times 3.65\ \mathrm{eV}\sqrt{[\sigma_N(e^-)]^2 + \frac{FE}{3.65\ \mathrm{eV}}}, \qquad (4)$$

where F is the Fano factor and E is the x-ray energy in eV. In the fitting procedure the Fano factor was kept fixed at the value of 0.155 reported in Ref. [18], while the σ_N parameter was let free. For the BI camera, the best fit was obtained for a σ_N of $15.3e^-$, a result which is in good agreement with our previous observation (i.e., $12.2e^-$). In the case of the FI camera, calculations with a Fano factor of 0.155 and a σ_N of $13.2e^-$ (determined from the histograms) yield a poor agreement between the computed curve and the observed FWHM values. In order to fit the data properly, an energy-dependent factor was added under the root of Eq. (4) to account for the imperfect CTE. In this factor a linear energy dependence was assumed. The calculated curves are shown in Fig. 12 by the red solid lines.

Finally, from the above histograms the lowest energy that can be measured with the von Hamos spectrometer was estimated for each camera. Low energy limits of 950 eV for the FI camera and 450 eV for the BI one were obtained.

C. Charge splitting effect

The photon energy dependence of the charge splitting effect was determined for both CCD cameras. The results are presented in Fig. 13. As shown, the relative number of single pixel events varies as a function of the photon energy in an opposite way for the two CCDs. It can be seen that for the FI camera almost all of the detected events are confined to a single pixel for low energy x rays. When the photon energy increases, a slight decrease in the relative number of single event pixels is observed. At the highest measured energy (17.479 keV) about 20% of all events are split between 2 to 4 pixels. However, for energies below 2 keV the number of single event pixels could not be determined because the split charge was lost in the background noise due to the poor charge transfer efficiency. A different behavior of the charge splitting effect can be seen for the BI CCD. In the

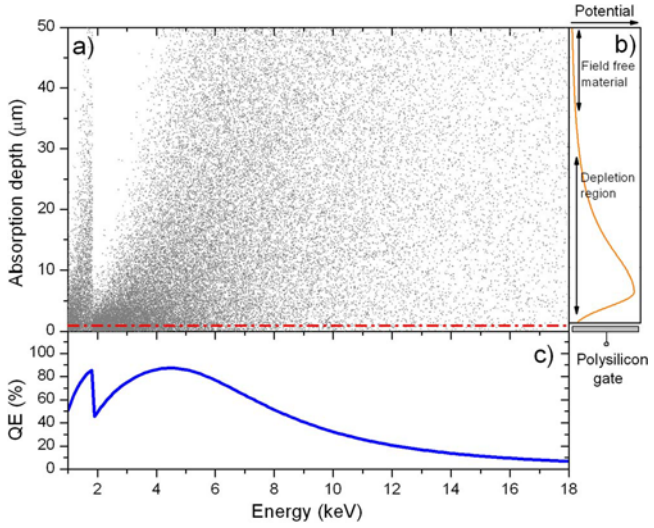

FIG. 14. (Color online) Results of Monte Carlo simulations of photon absorption in the FI CCD. (a) Depth absorption as a function of the photon energy (each point corresponds to an absorption event). (b) Schematic variation of the electrostatic field across the pixel depth. (c) Ideal quantum efficiency derived from the analytical formula (see text).

photon energy range from 1 to 1.84 keV (K-absorption edge of Si) an increase in the number of detected single event pixels is observed. For x-ray energies just above 1.84 keV the number of single event pixels decreases drastically to a very low level of less than 1% of the total number of detected events. This fact signifies that almost all events are split across several pixels. When the x-ray energy is further increased the number of single events increases and for energies above 6 keV the ratio of the single events to the split events reaches a constant level of 45%.

To better understand the photon energy dependence of the charge splitting effect Monte Carlo simulations of the photon absorption in the CCDs were performed. Results are presented in Fig. 14(a) for the FI camera and in Fig. 15(a) for the BI one. The Monte Carlo simulations were computed employing an exponential probability distribution,[3]

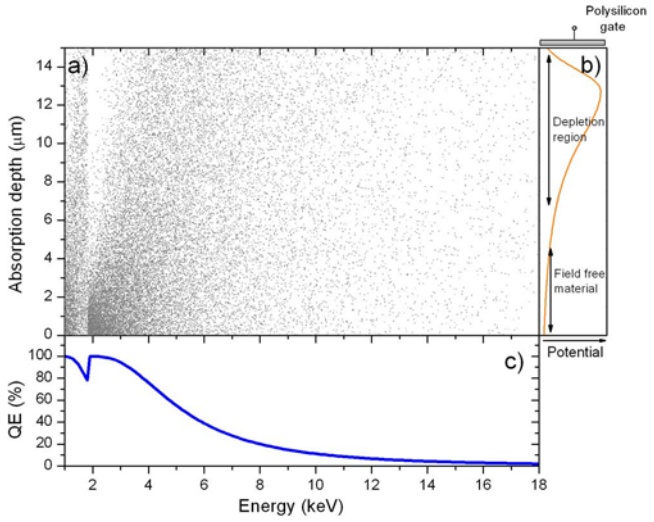

FIG. 15. (Color online) Same as Fig. 14 but for the BI CCD.

$$x_i = -L_x(E)\log_e(N_r), \quad (5)$$

where $L_x(E)$ is the absorption length in silicon for a given x-ray energy and N_r is a random number between 0 and 1. The calculated x_i correspond to the depth at which a photon of given energy is fully absorbed as a result of the photoelectric effect. The computation was performed with a 10 eV photon energy step and for each step 1000 events were generated.

In Figs. 14(b) and 15(b) the schematic pixel potential well profiles are shown (orange lines). Depending on the strength of the electric field two regions can be distinguished: a field-free material and a depletion region. By design, in the case of front-side photon illumination, photons fall on the front surface where the gates are located, whereas for back-side photon illumination x rays enter the back surface farthest from the gates. Therefore, with respect to the direction of incident photons, these regions are located in an opposite way for FI and BI cameras. As already discussed in Sec. II, for the FI camera x rays penetrating the gate and oxide structure [marked as a red dashed line in Fig. 14(a)] may be absorbed before entering the depletion region and the field-free material. In the case of the BI camera, x-rays enter the field-free material first and then the depletion region. From the Monte Carlo simulations for the BI camera one can see that for photon energies slightly above the K-absorption edge of Si (i.e., 1.84 keV) almost all x rays are absorbed within a depth of 3–4 μm where the electric field is weak. Therefore, at these energies most of the generated electrons can diffuse thermally to neighboring pixels before being trapped in the potential well of one pixel. This assertion agrees with the results presented in Fig. 13, where for energies just above 1.84 keV the number of single events is close to zero. As the photon energy increases photon absorption takes place directly in the depletion region.

For the FI camera, our experimental results for the degree of charge splitting as a function of the photon energy are also confirmed by the Monte Carlo simulations. At low energies almost all of the incident x-ray photons are absorbed directly in the depletion region where the electric field is strong enough to prevent thermal diffusion of the electron cloud. Therefore, in comparison with the BI CCD, the charge splitting effect is weak. However, the number of split charge events increases at higher photon energies due to the larger penetration depth. As a result, photoabsorption takes place beneath the depletion region, where again due to the weak electric field the charge can diffuse to adjacent pixels.

The charge splitting can also take place when a photon is absorbed on the pixel boundary. However, since the size of the charge cloud is extremely small in comparison to the pixel sizes (20×20 μm^2 for the BI CCD and 27×27 μm^2 for the FI), this effect does not play a significant role. The estimated size of the charge cloud for a photon energy of 1 keV is about 0.005 μm and for an energy of 17.5 keV about 1 μm.[19] Consequently, the contribution of the split charge created when the photon is absorbed at the boundary of the pixels to the total number of observed split charges will be on the level of only a few percent for the highest measured energy.

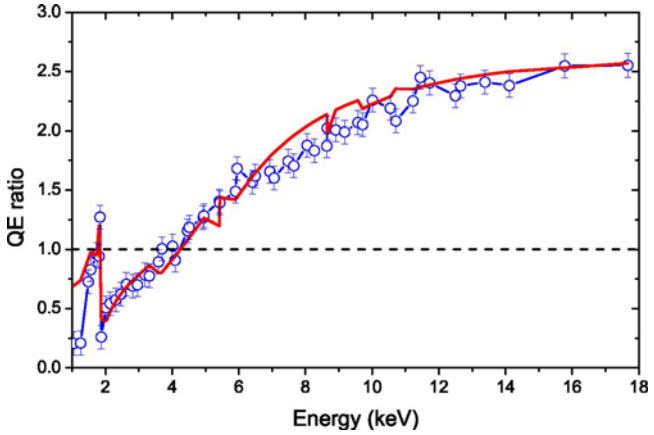

FIG. 16. (Color online) Measured QE ratios of front- to back-illuminated CCDs as a function of the incoming photon energy (blue open circles). Results of theoretical calculations are also shown (red solid line).

D. Quantum efficiency ratio of the front- and back-illuminated CCDs

In Figs. 14(c) and 15(c) the ideal quantum efficiencies as a function of incoming photon energy are shown. The QE curves were calculated employing the analytical formulas (1) and (2) and using the absorption coefficients reported in Ref. 20. We assumed that the CCE is equal to 1 and that there are no losses due to photon reflection on the Si chip surface. The calculated QE curves show two important characteristic features. First, as the photon energy approaches the K-absorption edge of Si a completely different behavior in the QE of the FI and BI cameras is seen. For the FI CCD a strong absorption in the dead layer structure decreases the QE, while in the case of the BI camera an increase in the efficiency is observed. Secondly, even in an ideal case, due to the absorption in the dead layer structure, the QE of the FI camera would be less than 100%.

In order to derive the experimental QE ratios, the intensities of the measured x-ray characteristic lines were fitted by means of a least-square method employing Voigtian functions. Examples of such fits were already shown in Figs. 3 and 4. Because the experimental setup was identical for the measurements performed with the FI camera and the BI one, the ratio of the fitted intensities corresponds to the QE ratio of the two cameras at a given x-ray energy. In Fig. 16 the measured QE ratio of the FI to the BI CCDs as a function of the photon energy is depicted by blue open circles and the horizontal dashed line corresponds to a QE ratio of 1. These results show that for photon energies above 4.5 keV the FI CCD is more efficient than the BI one and at the highest measured energy the QE ratio is equal to 2.55. In the low energy range the QE of the BI camera is significantly higher. For a photon energy of 1.872 keV just above the Si K edge, corresponding to the Sr $L\beta$ line, the detection efficiency of this camera is higher by a factor of 3.84.

The experimentally derived QE ratios were fitted with a theoretical model based on the analytical formulas (1) and (2). The values of R and CCE were assumed to be the same for both CCDs. Since x-ray radiation is incident on the CCD surface with an angle depending on the measured x-ray energy and the crystal, a correction factor A was added. In fact,

this angle of incidence corresponds to the Bragg angle. Therefore, the theoretical formula for the QE ratio can be written as follows:

$$\mathrm{QE}(E)_{\mathrm{ratio}} = \frac{(e^{-X_{\mathrm{FI}_{\mathrm{SiO_2}}}A(E)}) \times (1 - e^{-X_{\mathrm{FI}}A(E)})}{1 - e^{-X_{\mathrm{BI}}A(E)}},$$

$$\text{with } A(E) = \frac{2dE(\mathrm{keV})}{12.398nL_A(E)}. \quad (6)$$

where $X_{\mathrm{FI}_{\mathrm{SiO_2}}}$ is the thickness of the dead layer structure in the FI camera and X_{FI} and X_{BI} are the depletion depths for the FI and the BI cameras, respectively. L_A stands for the absorption length in silicon for a given energy E, whereas n is the reflection order and $2d$ are the lattice constants of the crystals given in Table I.

Formula (6) was used to fit the experimental data of the QE ratio. The result is shown as a red solid line in Fig. 16. As it can be seen, except below 1.5 keV, the computed curve reproduces the energy dependency of the measured QE ratios well. In particular, the Si K-edge absorption effect at 1.84 keV is well reproduced by the calculations. The small "jumps" observed in the theoretical curve correspond to abrupt changes of the Bragg angle from $\sim 25°$ to $\sim 60°$ when replacing the crystal of the spectrometer for measuring higher x-ray energies. As a result of the Bragg angle change, the thickness of the CCD chip seen by the photons becomes suddenly smaller than the one corresponding to the measurements performed with the previous crystal, which leads to the observed small dips in the theoretical QE ratio curve.

The best fit of the theoretical function given by formula (6) to the experimental data was obtained for the following values of the fitting parameters: $X_{\mathrm{FI}_{\mathrm{SiO_2}}} = 1\ \mu$m, $X_{\mathrm{FI}} = 40\ \mu$m, and $X_{\mathrm{BI}} = 15\ \mu$m. The results found for the depletion depths are in good agreement with the values given by the manufacturer (see Table III). For the dead layer thickness of the FI camera, there is no indication in the CCD data sheet but the obtained result agrees reasonably well with the thicknesses reported for other similar CCD cameras.[12,21]

As the QE ratios of the two cameras can be reproduced well with Eq. (6) derived from formulas (1) and (2), one could conclude that it should be possible, using the same formulas, to determine the absolute QE of the investigated CCDs. However, to this end the CCE should be known. As this parameter which depends on the photon energy is not provided by the manufacturer, it should be determined experimentally. With the setup employed in the present study, this would represent a difficult task because absolute x-ray intensities are not easy to determine with a crystal spectrometer, with some parameters such as the crystal reflectivity being poorly known. Note that because it was assumed that the CCE is the same for both CCDs, this quantity cancels out in the QE ratio formula and only the well known photon absorption coefficients are needed.

IV. SUMMARY

In conclusion, a variety of characteristic x-ray emission lines were measured with a high-resolution von Hamos curved crystal spectrometer using for the detection of the diffracted x-rays a FI CCD camera and a BI one. From the acquired data the energy response of the two cameras was found to be well linear for both detectors over the energy range between 1 and 18 keV. The charge splitting effect was probed as a function of the incoming photon energy and the CCD type. Obtained results could be explained with Monte Carlo simulations. Finally, the QE ratio of the FI to BI camera was determined and compared with theoretical predictions. A good agreement was observed over the whole energy range.

ACKNOWLEDGMENT

The financial support of the Swiss National Science Foundation is acknowledged.

[1] W. Boyle and G. Smith, Bell Syst. Tech. J. **49**, 587 (1970).
[2] W. Boyle and G. Smith, US Patent No. 3792322 (February 12, 1974).
[3] J. R. Janesick, *Scientific Charge-Coupled Devices* (SPIE, Washington, 2001).
[4] P. Plucinsky *et al.*, Proc. SPIE **5488**, 251 (2004).
[5] C. D. Mackay, Annu. Rev. Astron. Astrophys. **24**, 255 (1986).
[6] J. T. Bosiers, I. M. Peters, C. Draijer, and A. Theuwissen, Nucl. Instrum. Methods Phys. Res. A **565**, 148 (2006).
[7] M. Bregant and E. Milotti, Nucl. Instrum. Methods Phys. Res. A **413**, 479 (1998).
[8] www.fairchildimaging.com
[9] www.roperscientific.com
[10] www.andor.com
[11] www.e2v.com.
[12] A. Owens, Nucl. Instrum. Methods Phys. Res. A **529**, 391 (2004).
[13] J. Hoszowska, J.-Cl. Dousse, J. Kern, and Ch. Rheme, Nucl. Instrum. Methods Phys. Res. A **376**, 129 (1996).
[14] R. D. Deslattes, E. J. Kessler, P. Indelicato, L. de Billy, E. Lindroth, and J. Anton, Rev. Mod. Phys. **75**, 35 (2003).
[15] ST133 Princeton Instruments manual.
[16] N. Saks, IEEE Electron Device Lett. **EDL-1**, 131 (1980).
[17] www.amptek.com
[18] A. Owens, G. W. Fraser, and K. J. McCarthy, Nucl. Instrum. Methods Phys. Res. A **491**, 437 (2002).
[19] K. J. McCarthy, A. Owens, A. D. Holland, and A. A. Wells, Nucl. Instrum. Methods Phys. Res. A **362**, 538 (1995).
[20] http:/physics.nist.gov/xcom
[21] M. Pivovaroff, S. Jones, M. Bautz, S. Kissel, G. Prigozhin, G. Ricker, H. Tsunemi, and E. Miyata, IEEE Trans. Nucl. Sci. **NS-45**, 164 (1998).